PHYSICAL REVIEW B **91**, 144103 (2015)

First-principles study of the phonon modes in bismuth sillenites

D. J. Arenas,[1,2,*] Carl Middleton,[1] and A. F. Kemper[3]
[1]*Department of Physics, University of North Florida, Jacksonville, Florida 32224, USA*
[2]*Institute of Scientific and Industrial Research, Osaka University, 8-1 Mihogaoka, Ibaraki, Osaka 567-0047, Japan*
[3]*Computational Research Division, Lawrence Berkeley National Laboratory, Berkeley, California 94720, USA*

(Received 6 January 2015; revised manuscript received 3 March 2015; published 9 April 2015)

Density functional theory calculations of the vibrational modes of $Bi_{12}SiO_{20}$ are presented, with a detailed assignment and geometry investigation of the vibrational modes in the sillenite structure. We show that the symmetry and geometry of the strong Raman peaks allow direct probing of the Bi-O(1) and Bi-O(2) bonds. The physical significance of the vibrational modes is considered to discuss experimental data on the trivalent sillenites and show evidence of O(1) and/or O(2) vacancies in the Bi-O framework. The infrared modes are also discussed to motivate future systematic studies of sillenites. The Born effective charges of sillenites are studied and the results show the existence of large and anisotropic charges. The magnitude of the LO-TO splits is also calculated and compared with experiment.

DOI: 10.1103/PhysRevB.91.144103 PACS number(s): 63.20.dk, 78.30.−j

I. INTRODUCTION

The sillenites $Bi_{12}SiO_{20}$ and $Bi_{12}GeO_{20}$ have been extensively studied for decades due to their numerous nonlinear-optic properties [1–4]. The crystal structure of these sillenites is the simplest in the family and can be referred to as the ideal sillenite structure. $Bi_{12}TiO_{20}$ has also gained recent interest not only for nonlinear applications [5,6] but also for its photocatalytic activity [7–9]. For the latter application the iron sillenite $Bi_{25}FeO_{39}$ has also received recent attention [10,11]. The synthesis and characterization of new sillenites remains an active research topic [12–18].

The simplest description of the sillenite structure is a bcc arrangement of MO_4 tetrahedra connected by a bismuth-oxygen framework. The center of each tetrahedron houses a metal cation M (e.g., Si^{4+}, Ge^{4+}). All bismuth atoms occupy sites with equivalent symmetry, while the oxygen atoms have three equivalent sites. O(1), the least symmetric site, has one bismuth atom as its nearest neighbor; O(2) has three bismuth nearest neighbors; and O(3) oxygen atoms form the tetrahedra. (See Table I and Fig. 1.) If the metal cation is not tetravalent, the resulting structure is more complex and depends on the valence number of the cation. Although there are conflicting views, the latest stoichiometry model of sillenites, by Valant and Suvorov [20], assumes partial occupation of Bi^{3+} cations in the center of the tetrahedron (M site), and the occupation percentage depends on the valence of the metal cation. For example, sillenites with trivalent metal cations (i.e., Ga^{3+}, Fe^{3+}) result in 50% Bi^{3+} occupation of the M site [20]. The lone pair of Bi^{3+} then creates an oxygen vacancy in the tetrahedron due to the large size of the lone pair [20].

Vibrational spectroscopy continues to be useful in understanding the electronic and structural properties of many compounds: from traditional [21] and novel superconductors [22–25] to multiferroics [26–28] and dielectrics [29,30]. Although the assignment of Raman and IR peaks can be difficult for some compounds, careful assignment can improve understanding of the structure. Detailed assignment of vibrational modes in Bi pyrochlores have resulted in several insights [31]; the spectra reveal relaxation of the selection rules due to displacement disorder [29,31,32], and the spectra can be used to study the effects of the displacement disorder on the tunability of the permittivity [33].

In this work, we report density functional theory (DFT) calculations of the infrared (IR) and Raman spectra of sillenites. The first purpose is to understand the physical significance of the vibrational modes. IR and Raman spectra are more useful if one understands the geometry of the vibrations. We made a careful comparison of different functionals to be able to correctly assign the experimentally observed IR and Raman modes. The analysis shows that the vibrational spectra can provide information on specific components of the sillenite structure. Only the vibrational spectra of the tetravalent and "ideal" sillenites $Bi_{12}SiO_{20}$ and $Bi_{12}GeO_{20}$ were investigated. The vibrational spectra of trivalent sillenites with random occupations would prove too difficult due to the large calculation times it would require to build large enough supercells that mimic true random occupation of M sites and O(3) vacancies [34]. Although it is difficult to prove using expensive DFT calculations, a physical argument is that the geometry of the vibrations should be very similar for the tetravalent and the trivalent sillenites since the substitutions and vacancies in the trivalent sillenites are random and correspond to (on average) one atom per unit cell of 33 atoms. In other words most modes such as "stretching of the Bi-O(1) bond" should have similar geometries for both tetravalent and trivalent sillenites. The experimentally similar spectra of trivalent and tetravalent sillenites in Ref. [31] give validity to this argument. Knowledge of the geometry of the modes proves useful in a comparison of the experimentally observed modes across different sillenites. The comparison shows that the trivalent sillenites deviate from the tetravalent sillenites at not only the tetrahedra, but also at the surrounding Bi-O framework. As will be discussed later in the text, one possibility is the existence of oxygen vacancies in the bismuth-oxygen framework of trivalent sillenites ($Bi_{25}GaO_{39}$, $Bi_{25}FeO_{39}$, and $Bi_{25}InO_{39}$).

The second purpose was to investigate the origin of LO-TO splitting in $Bi_{12}SiO_{20}$. Our calculations show highly anisotropic and anomalously large Born effective charges associated with the bonds between Bi-O(1) and Bi-O(2). This

---

[*] Corresponding author: djarenas@mit.edu

TABLE I. Wyckoff table for the silicon sillenite structure. Using simple-cubic translational vectors, 66 atoms are generated by applying 24 symmetry operations where two are always related by a simple bcc translation.

Site	*x*	*y*	*z*	Wyckoff site	Occupancy
Bi	0.32	0.18	0.02	24f	1
Si	0	0	0	2a	1
O(1)	0.37	− 0.01	0.26	24f	1
O(2)	0.20	0.20	0.20	8c	1
O(3)	− 0.095	− 0.095	− 0.095	8c	1

is an interesting result since most studies of large Born effective charges deal with ferroelectric compounds in polar space groups [35–37], while the the sillenites are well known to be in a nonferroelectric space group.

The third purpose was the opportunity to expand the literature on phonon calculations of metal oxides. The unit cell of the sillenites is large, and thus computations are expensive; we therefore present careful discussions on the convergence of important physical values. Also, although recent papers have used the LDA functional and claimed superiority over the GGA functional in some metal oxides [38], our results for sillenites show that GGA outperforms LDA in calculating the lattice parameters and bond lengths. Also, by using two different functionals for the calculation, we can improve the confidence in the understanding of the geometry and physical significance of the vibrational modes.

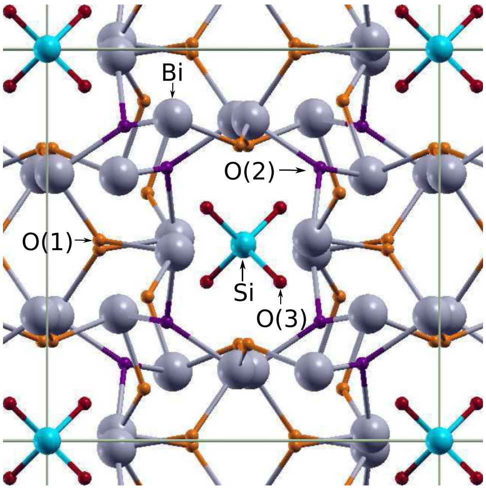

FIG. 1. (Color online) A representative sillenite structure. An *M* cation, such as Si^{4+} (blue), sits on the most symmetric site (2a) that corresponds to the edges and the center of the bcc cell. Each *M* cation is surrounded by four O(3) oxygens (red) in a tetrahedron configuration. Both O(2) and O(3) sit on 8c symmetric sites where O(2) (purple) are located farther from the 2a sites. The O(2) oxygens have three nearest-neighbor bismuth ions, which later in the text will be referred to as a Bi_3 plane for the discussion of some phonon modes. The bismuth (gray) and O(1) oxygen (orange) atoms sit on 24f sites, the least symmetric. Bi and O(1) are each other's nearest neighbors but each O(1) has another very close bismuth bonded to it. The Bi, O(1), and O(2) atoms form what is commonly called a "bismuth-oxygen" framework that interconnects the M-$O(3)_4$ tetrahedra. The image was created using the XCrySden program [19].

The paper has been divided into four mostly independent sections. The first section presents the details of the DFT calculations and includes discussion about convergence, and a comparison of LDA and GGA. The second section presents the assignment of the Raman modes, the comparison of the Raman spectra across different sillenites, and the evidence for O vacancies in the Bi-O framework. The third section presents the calculations on the strong IR modes, the anomalous Born effective charges, and LO-TO splitting. Finally, the last section discusses how the DFT calculations contrast and complement lattice dynamical calculations that fit spring constants, or potential parameters, to known vibrational spectra. This section also discusses future work.

II. DFT CALCULATION DETAILS

A. Unit cell

The sillenite structure occurs in the body-centered $I23$ space group, and has 33 atoms in the unit cell. (See Table I.) The site with highest symmetry is the *M* site since only one atom is generated by the operations. O occurs on two equally symmetric sites, the O(3) site which generates the four atoms in the tetrahedron, and the O(2) site, which generates four O ions each bonded to three nearest-neighbor Bi atoms. The least symmetric sites are those of Bi and O(1) with degeneracy 12 inside the Bi-O framework. In crystallography, it is customary to use a simple cubic unit cell with 66 atoms. Both choices of the unit cell yield the same physical crystal when translated. The larger supercell is useful for doping studies [7]. It is important to note, however, that only the bcc unit cell (and its translation vectors) yields the minimal-volume Brillouin zone. Therefore only 33 atoms should be used in a phonon calculation; using a larger unit cell results in nonphysical modes.

B. Energy calculations

Energy calculations were carried using the open-source DFT software Quantum Espresso [39]. For comparison, we used two norm-conserving pseudopotentials: a Perdew-Burke-Ernzerhof (PBE) GGA functional [40] and a Perdew-Wang (PW) LDA functional. Structural calculations using the GGA functional were performed using both the $6s^2\,6p^3$ and $5d^{10}\,6s^2\,6p^3$ valence states for Bi. The calculated lattice parameters from the $6s^2\,6p^3$ state agreed better with experiment (0.1% agreement compared to 2%). Due to the better results of the structural calculations of our system, unless otherwise noted, all results presented in this work use the $6s^2\,6p^3$ valence state for Bi.

Unless otherwise noted, all calculations used an energy cutoff of 100 Ry for the expansion of plane waves in the self-consistent calculation. A 100 Ry cutoff is higher than the value used in other studies of sillenites in the literature [41–43] and comparable to values used for phonon calculations of pyrochlores [44,45]. The convergence versus cutoff energy will be discussed when we present interesting physical quantities.

A $3 \times 3 \times 3$ mesh of *k* points in the Brillouin zone was generated using the Monkhorst-Pack scheme [46]. At this *k*-mesh density, considering the large unit cell, the lattice parameter converged within less than 0.01% for both functionals and the phonon frequencies are converged within less than 1 cm^{-1} for all modes.

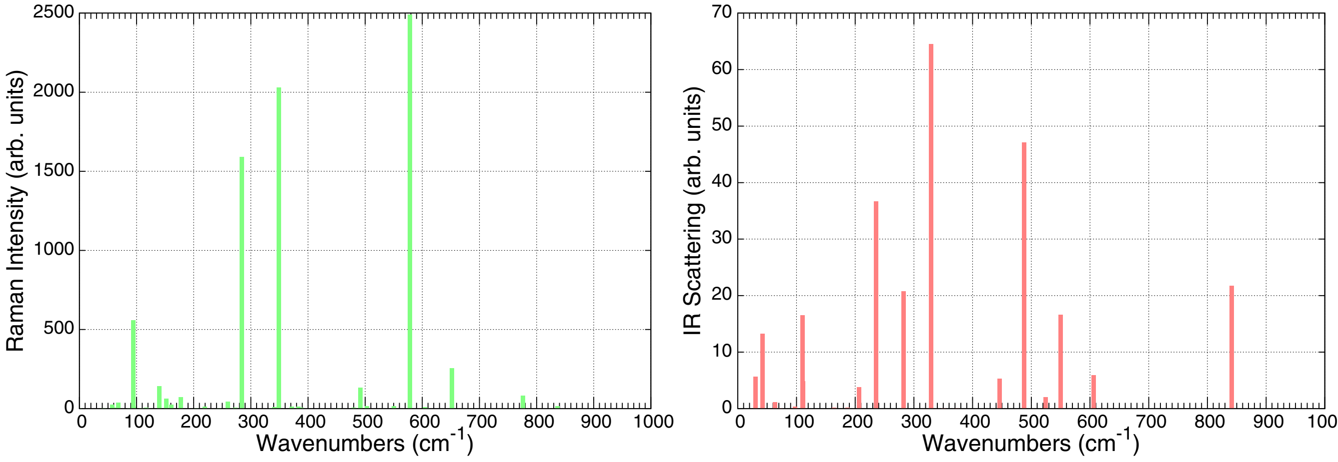

(a) (b)

FIG. 2. (Color online) Raman and IR scattering cross sections calculated using the LDA functional. The intensity of the modes was taken into consideration in the assignment of the modes.

C. Optimization of the unit cell

The minimum energy configuration of the crystal was investigated by two approaches, a manual variation of the lattice constant followed by relaxation of internal coordinates, and a constrained minimization of the stress tensor. The results, using the GGA functional, agreed on the final lattice constant (10.12 Å) to within 0.1%. For both functionals, the convergence of the lattice parameter versus the kinetic-energy cutoff for the plane waves was better than 0.1%.

Using the GGA functional, the calculated lattice parameter compares well with the experimentally observed value for $Bi_{12}SiO_{20}$ (10.12 Å [41]). The LDA functional predicted a 9.78 Å lattice constant, an underestimation of the lattice constant common in LDA calculations and previously reported in pressure-dependent calculations of $Bi_{12}SiO_{20}$ [41]. The results were similar for $Bi_{12}GeO_{20}$, where the experimental lattice constant (10.14 Å) [20,47] is closer to the value obtained from the GGA functional (10.17 Å), rather than the LDA functional (9.81 Å). For $Bi_{12}SiO_{20}$, the bond experimentally measured by Wiehl *et al.* was compared to our DFT calculations [41]. The bond lengths calculated from the GGA functional were accurate within about 1% and outperformed LDA. (See Table S1 in the Supplemental Material [48].)

The pseudopotential comparison is not trivial since it has been reported that calculations for metal oxides of the lattice parameter and bond lengths agree better with experiment for LDA than for GGA [38]. Although LDA yielded accurate lattice constants in calculations of the $Bi_2Ti_2O_7$ pyrochlore [38] and other pyrochlores [49], our results for sillenites are similar to calculations of other systems where LDA underestimates cell parameters more than GGA does [50–52].

D. Phonon calculations

The vibrational frequencies were calculated in the linear response regime using density functional perturbation theory (DFPT). The “crystal” acoustic sum rule (ASR), which takes into account both the sum rule and the index rule [53,54], was imposed on the calculated dynamical matrix. The infrared

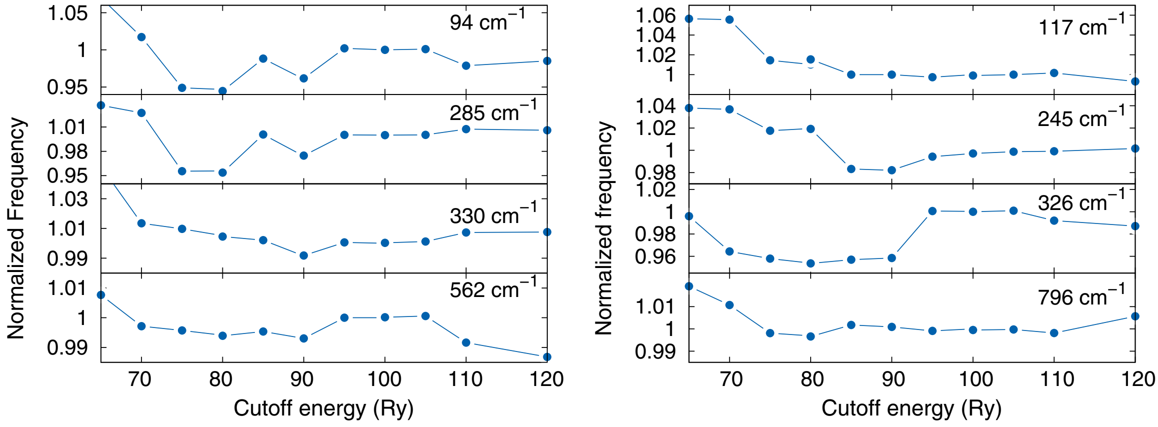

(a) (b)

FIG. 3. (Color online) Frequency of the phonon modes versus the cutoff energy of the plane-wave expansion. Panel (a) shows a few of the strong Raman modes while (b) shows some strong IR modes. Many reports on metal oxides use cutoff energies between 70–90 Ry since higher cutoff energies result in calculations that are too long. This convergence study shows that the calculated phonon frequencies can have an inaccuracy as much as 5–10 cm^{-1} in some modes. All frequencies plotted are after imposing the crystal ASR.

TABLE II. Comparison of the Raman and IR modes of Bi$_{12}$SiO$_{20}$ with the DFT calculations using the PBE-GGA and PW-LDA functionals. The calculations are compared to the experimental values from Refs. [56], [47], and [57]. The optical activity of the modes was useful in the assignment of the modes: A and E are Raman active but IR inactive while the F modes are active on both. The most pronounced Raman and IR modes in the experimental spectra are marked with $^{\dagger R}$ and $^{\dagger IR}$, respectively; the geometries of IR/Raman modes that may be useful for comparison across sillenites are described. All reported DFT frequencies are after application of the "crystal" acoustic sum rule to the dynamical matrix. $^{(?)}$ marks modes with difficult assignment due to different geometries predicted from LDA and GGA and/or proximity of various modes with similar symmetries and calculated intensities.

Bi$_{12}$SiO$_{20}$					
Raman freq. [56] (cm^{-1})	Raman freq. [47] (cm^{-1})	IR freq. [57] (cm^{-1})	DFT: GGA (cm^{-1})	DFT: LDA (cm^{-1})	Assignment
44	44		$33^?$	$30^?$	F
58	56		52	43	$F^{\dagger R}$
68	65		58	68	E
92	88		94	92	$A^{\dagger R}$: Mostly O(2) breathing and Bi and O(1) movement
89	88	89	83	73	F
99	98	99	$95^?$	$98^?$	F
106	n.o.	107	111	111	$F^{\dagger IR}$: M-O$_4$ tetrahedron displacement
114	n.o.	115	102	111	F
132	129		129	140	$E^{\dagger R}$: Bi and O(1) atoms shear the framework
135	n.o.	136	$117^?$	$121^?$	$F^{\dagger IR}$: M-O$_4$ tetrahedron displacement. Bi-O(1) move together
149	144		142	152	A
174	n.o.	175	164	163	F
171	167		184	177	A
196	n.o.	195	$205^?$	$187^?$	F
209	205	208	$218^?$	$206^?$	F
238	n.o.	237	245	235	$F^{\dagger IR}$: Mostly Bi-O(1) and Si-O(3) bending
252	n.o.		260	260	E
282	277		285	282	$A^{\dagger R}$: O(2) atoms breathe away from the nearby Bi$_3$ plane
n.o.	n.o.	288	276	282	F
n.o.	n.o.	314	326	330	$F^{\dagger IR}$: Mostly displacement of Si^{+4} opposite to all O(2) atoms
331	328		330	349	$A^{\dagger R}$: O(1) bend the Bi-O(1) bond
352	351	353	371	374	F
n.o.	n.o.	462	472	488	$F^{\dagger IR}$: Mostly O(2) movement in the nearby Bi$_3$ plane
464	458		465	492	E
n.o.	n.o.	531	535	549	$F^{\dagger IR}$: O(2) and O(1) movement
546	538		562	579	$A^{\dagger R}$: O(1) move and stretch the Bi-O(1) bond
n.o.	n.o.	579	590	602	F
n.o.	n.o.	609	604	606	F
626	621		637	652	E: Mostly stretching of the Bi-O(1) bond
785	787		743	777	A: Symmetric stretch of the M-O$_4$ tetrahedron
827	n.o.	822	796	841	$F^{\dagger IR}$: Asymmetric stretch of the M-O$_4$ tetrahedron

cross sections were calculated within the linear response by analyzing the induced dipole for each phonon calculation. The Raman cross sections were calculated using the second-order response method by Lazzerri and Mauri [55]. Figure 2 shows the calculated scattering cross sections for Raman and IR.

The convergence of the phonon modes versus the cutoff energy of the plane waves was not trivial. Figure 3 shows representative phonon modes for Raman (a) and IR (b) calculated from GGA. Our results show that some phonon modes converge to a value rather quickly while others show an uncertainty as high as 3%. The convergence of the calculations for both functionals was more than satisfactory for the assignment of the Raman modes, and the geometry of the vibrational modes versus the cutoff energy was also carefully investigated. The predicted IR and Raman intensities converged even more slowly; however, at 100 Ry and the k mesh described earlier, it was possible to discern the relative intensities. Overall, the accuracy of the calculations was satisfactory for all the conclusions presented in this paper.

E. Pseudopotentials

The justification to use two different functionals is twofold. First, for metal oxides, there are very few comparison studies. Earlier studies on Bi$_2$Ti$_2$O$_7$ used an LDA functional and claimed that LDA works better for metal oxides in the estimation of lattice constants. The authors [38] reference two publications [50,51] by Wu *et al*; in these two papers it is shown that LDA outperforms GGA for BaTiO$_3$ and PbTiO$_3$; however, one can also see that GGA outperforms LDA in other compounds such as MgO [50], and KTaO$_3$ and KNbO$_3$ (Tables II and VI in Ref. [51]). Recently, DFT phonon studies on other pyrochlores also choose LDA over GGA [44,45], but the justification is based on a reference [49] that used

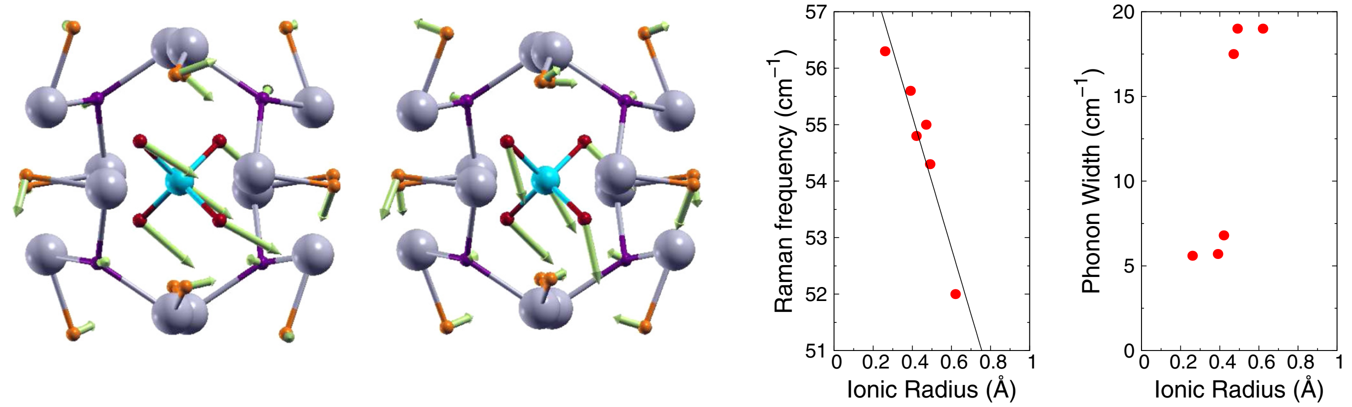

(a)PBE-GGA (b)PW-LDA (c) (d)

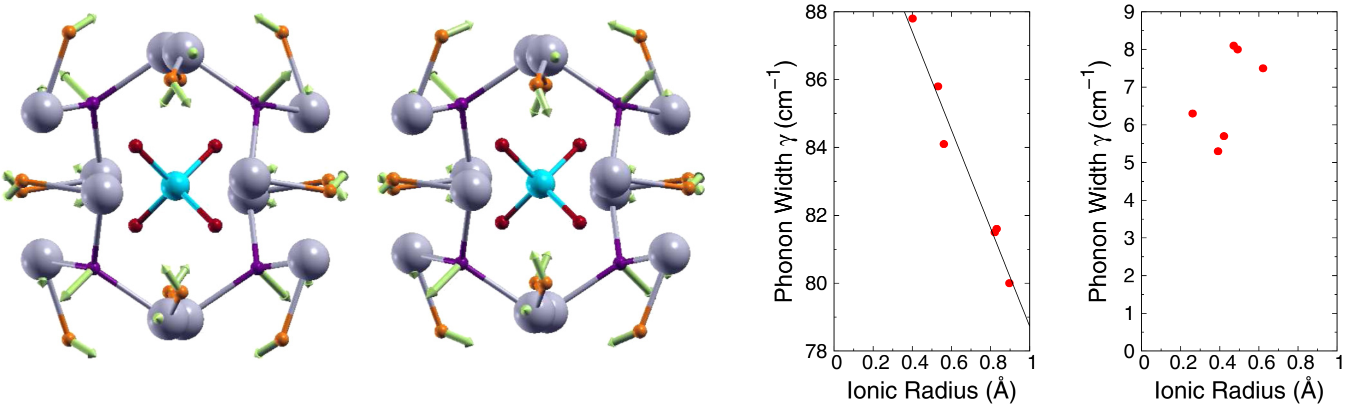

(e)PBE-GGA (f)PW-LDA (g) (h)

FIG. 4. (Color online) The Raman-strong 58 and 92 cm^{-1} modes. The 58 cm^{-1} F mode involves the movement of many atoms in both the Bi-O framework and tetrahedron and does not offer insight into any particular bond. The 92 cm^{-1} A mode mostly corresponds to O(2) breathing and Bi and O(1) movement. The geometries of the vibrations obtained from GGA [(a), (e)] and LDA [(b), (f)] calculations are shown. Si and Bi are denoted by blue and gray, respectively; O(1), O(2), and O(3) by orange, purple, and red. Green arrows denote the force on each atom. Using the experimental data from Ref. [47], the frequency [(c), (g)] and the width [(d), (h)] of the mode for six sillenites are plotted in increasing ionic radius of the M cation: $Bi_{12}Si^{+4}O_{20}$, $Bi_{12}Ge^{+4}O_{20}$, $Bi_{12}Ti^{+4}O_{20}$, $Bi_{25}Ga^{+3}O_{39}$, $Bi_{25}Fe^{+3}O_{39}$, and $Bi_{25}In^{+3}O_{39}$.

only LDA calculations. As previously stated, for our structural calculations on $Bi_{12}SiO_{20}$, the GGA functional outperformed the LDA functional (<1% compared to 3% deviation from experiment). In the phonon calculations, GGA also fared slightly better (Table II). However, the calculation should only be taken as one data point in the comparison between two functionals. Only as more and more calculations on large unit cell metal oxides are presented can we make stronger conclusions.

The second and most important justification is the dependence of phonon mode calculations on accurate energy calculations. The frequency and the geometry of the IFCs of each mode are dependent on the dynamical matrix and the corresponding second derivatives. An 80 Ry cutoff energy for the plane waves in the energy calculations resulted in convergence uncertainties around 0.01 Ry (150 meV). This is only 10^{-5} of the total energy, but as Fig. 3 shows, this still corresponds to uncertainties in the phonon frequencies higher than 10^{-2}. The internal force constants (IFCs) converge slowly and they require imposition of the sum rules. Since LDA and GGA are both approximations, it is more transparent to use both functionals to explore the geometry of the phonon modes. Therefore, for modes with important physical geometries, the results will be shown from each functional calculation to strengthen the validity of the conclusions. As a last note, when plotting the geometry of the modes we have chosen to show all atoms and their force constants so that it is clear which atoms are mainly responsible for the particular mode (see Figs. 4–6).

III. RESULTS AND DISCUSSION: RAMAN

The 33 atoms in the sillenite bcc unit cell result in 96 optical and 3 acoustic modes. The symmetry operations of the space group yield degeneracies in the frequencies of these modes. For the simple sillenite structure, the 99 modes are grouped in the A, E, and F (or T) representations as

$$\Gamma = 8A(R) + 8E(R) + 24F(R,IR) + F, \tag{1}$$

which means that there are 41 resonant frequencies. (For convenience we say "41 modes.") There is one F zero-frequency acoustic mode, and only the rest of the F modes are IR active. The A, E, and F modes are all Raman active.

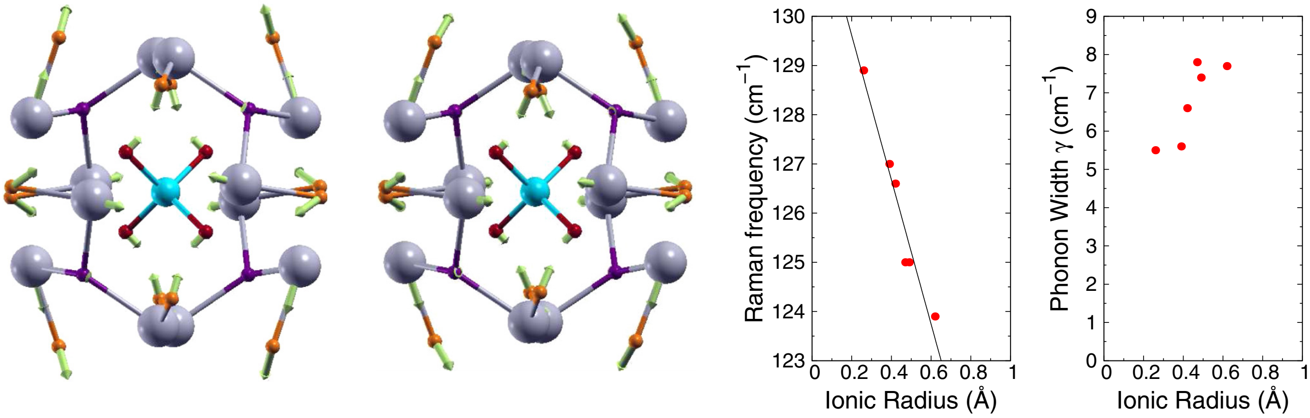

(a)PBE-GGA (b)PW-LDA (c) (d)

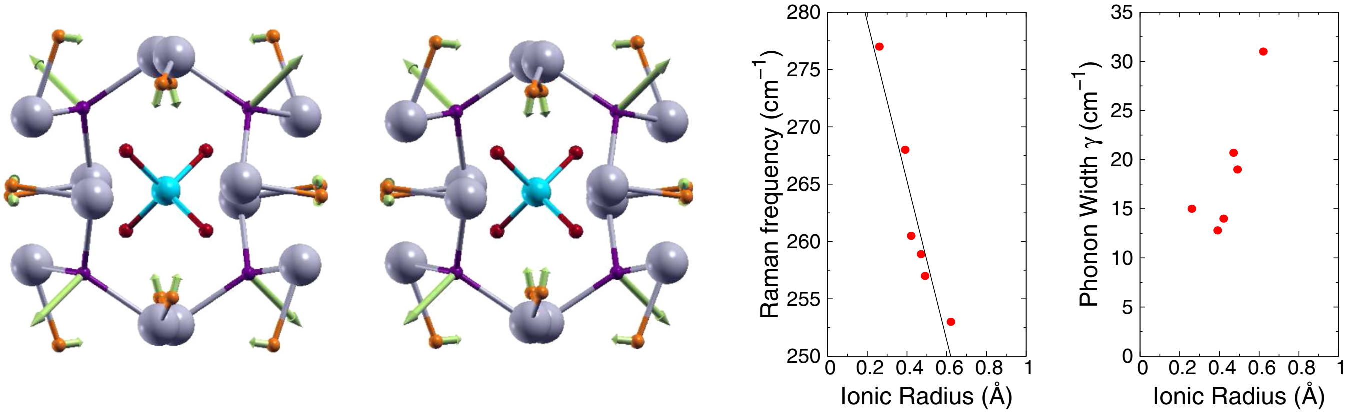

(e)PBE-GGA (f)PW-LDA (g) (h)

FIG. 5. (Color online) The Raman-strong 132 and 282 cm^{-1} modes. For the 132 cm^{-1} E mode Bi and O(1) atoms shear the framework. Note that the Bi and O(1) ions move in similar direction and therefore the frequency of the mode should not be as sensitive to the Bi-O(1) bond. The 282 cm^{-1} A mode corresponds to breathing of the O(2) atoms. The atoms breathe away from the center of the unit cell and the nearby Bi$_3$ plane. The geometries of the vibrations obtained from GGA [(a), (e)] and LDA [(b), (f)] calculations are shown. Si and Bi are denoted by blue and gray, respectively; O(1), O(2), and O(3) by orange, purple, and red. Green arrows denote the force on each atom. Using the experimental data from Ref. [47], the frequency [(c), (g)] and the width [(d), (h)] of the mode for six sillenites are plotted in increasing ionic radius of the M cation: Bi$_{12}$Si^{+4}O$_{20}$, Bi$_{12}$Ge^{+4}O$_{20}$, Bi$_{12}$Ti^{+4}O$_{20}$, Bi$_{25}$Ga^{+3}O$_{39}$, Bi$_{25}$Fe^{+3}O$_{39}$, and Bi$_{25}$In^{+3}O$_{39}$.

Table II shows the calculated phonon frequencies for Bi$_{12}$SiO$_{20}$. The table also shows the experimental Raman frequencies: 5 K data from single crystals [56] and room-temperature data from powder samples [47]. The latter data are also presented since the systematic study of various sillenite compounds in Ref. [47] was performed on these conditions. Table II also shows IR data at 90 K from Wojdowski *et al.* [57]. The assignment of the modes was not limited to choosing calculated frequencies that were closest to the experimental values. Such an assignment is not appropriate for this system since there are more than 20 experimental peaks in a range of 750 cm^{-1} and 40 calculated frequencies to choose from. Rather, we performed a careful assignment that uses the symmetry of the modes (A, E, and F) and comparison to the IR data. Although the LDA calculations overestimated the frequency of the modes, the intensity calculations (Fig. 2) which are not available for GGA functionals were important in identifying which mode geometries should be stronger in the Raman spectrum. It should be mentioned that since the frequencies calculated using LDA and GGA were different, extra care was taken in identifying the geometry of each mode so that the calculations could be compared to each other—a comparison based on closest frequencies would be erroneous in some of the modes.

A. Assignment and symmetries of the six strongest Raman modes

First, we will focus our discussion on the six strongest modes in the Raman. These modes are the easiest to track along different sillenite compounds and therefore offer the possibility for systematic studies. Apart from the lowest-frequency mode, the LDA calculations were successful in predicting these modes as the strongest Raman scatterers. As a note for this section, when we refer to a particular mode, we refer to the experimental frequency of Bi$_{12}$SiO$_{20}$ at 90 K (first column of Table II). The figures showing the comparison across different sillenites use the values from Ref. [47] where six sillenites were measured at 300 K in identical conditions.

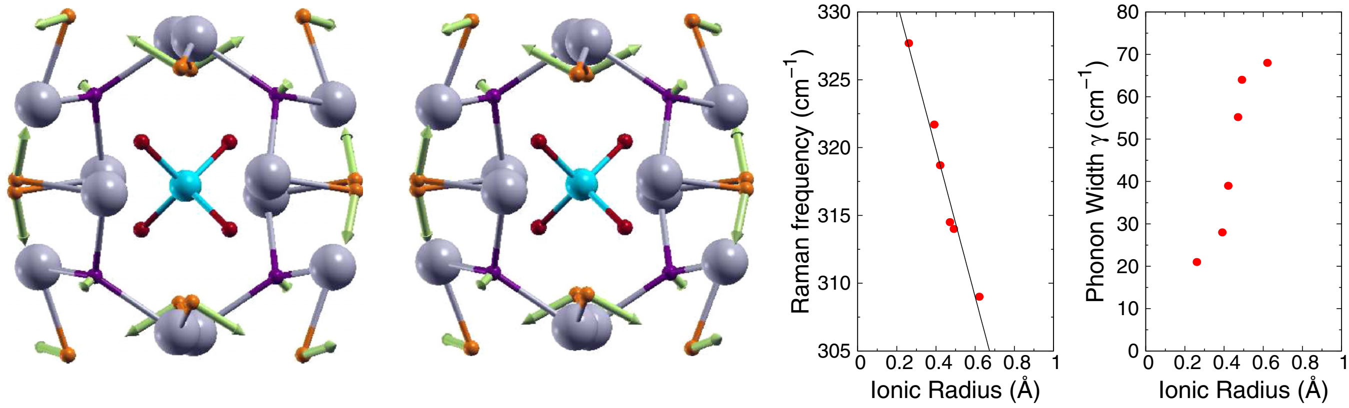

(a)PBE-GGA (b)PW-LDA (c) (d)

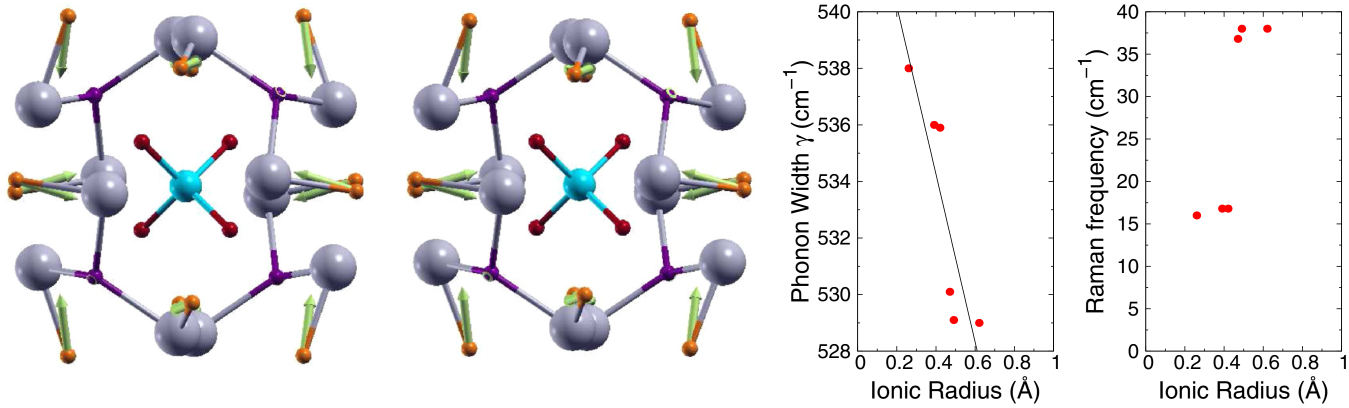

(e)PBE-GGA (f)PW-LDA (g) (h)

FIG. 6. (Color online) The Raman-strong 331 and 546 cm^{-1} modes. The 331 cm^{-1} A mode involves bending of the Bi-O(1) bond. This A mode presents important physical information because it involves mostly the bending force constant of Bi-O(1). The 546 cm^{-1} mode also probes the Bi-O(1) bond for it involves movement of the O(1) atoms to stretch the Bi-O(1) bond. The geometries of the vibrations obtained from GGA [(a), (e)] and LDA [(b), (f)] calculations are shown. Si and Bi are denoted by blue and gray, respectively; O(1), O(2), and O(3) by orange, purple, and red. Green arrows denote the force on each atom. Using the experimental data from Ref. [47], the frequency [(c), (g)] and the width [(d), (h)] of the mode for six sillenites are plotted in increasing ionic radius of the M cation: $Bi_{12}Si^{+4}O_{20}$, $Bi_{12}Ge^{+4}O_{20}$, $Bi_{12}Ti^{+4}O_{20}$, $Bi_{25}Ga^{+3}O_{39}$, $Bi_{25}Fe^{+3}O_{39}$, and $Bi_{25}In^{+3}O_{39}$.

The six most pronounced modes in the Raman offer the best opportunity to test the accuracy of the DFT calculations. Excluding the 58 cm^{-1} mode, the GGA calculations agreed with experiment by 3% and the average variance was around 1%. For LDA, the modes agreed by better than 6% and the average variance was less than 4%. (See Table II.) The remarkable agreement with experiment should justify future DFT studies of phonon modes in bismuth oxides.

1. 58 cm^{-1} Raman mode

The 58 cm^{-1} Raman mode is clearly visible across the six sillenites studied in Ref. [47]: $Bi_{12}SiO_{20}$, $Bi_{12}GeO_{20}$, $Bi_{12}TiO_{20}$, $Bi_{25}GaO_{39}$, $Bi_{25}FeO_{39}$, and $Bi_{25}InO_{39}$. Ramdas *et al.* showed in their single-crystal measurements that the symmetry of the mode is F [56]. Comparison to IR was not useful because the few IR studies on $Bi_{12}SiO_{20}$ and $Bi_{12}GeO_{20}$ do not report any modes below 90 cm^{-1} [57,58]. Figure 4 shows the symmetry of the 58 cm^{-1} Raman mode as well as the change in frequency and width of the mode across six different sillenites. The vibration involves both the tetrahedron and the Bi-O framework and therefore does not provide clear insight into any particular bond or structural region. As a side note, this was the only experimentally strong Raman mode that the calculations did not predict a high intensity for.

2. 92 cm^{-1} Raman mode

The strong Raman mode around 90 cm^{-1} is at first difficult to assign due to the proximity of many modes in the experimental [56] and computational results. An E (88 cm^{-1}) and A (92 cm^{-1}) mode, resolved at lower temperatures [56], are indistinguishable from each other at 300 K [47]. The DFT calculations also yield proximal E and A modes at 82 cm^{-1} and 94 cm^{-1}. DFT using GGA also predicts a 95 cm^{-1} F mode, but polarization measurements at low temperatures show that this mode is weaker than the aforementioned. Also, the calculations predict that the A mode has a stronger Raman scattering cross section. As shown in Fig. 4, this mode is mostly breathing of the O(2) atoms away from the Bi_3 plane and movement of the O(1) atoms.

3. 132 cm^{-1} Raman mode

The strong 132 cm^{-1} peak in the Raman is assigned to the 129 cm^{-1} E mode in the GGA calculations (Fig. 5). The assignment is straightforward due to the polarization properties and the lack of proximal strong modes [56]. DFT also predicts an F mode at 119 cm^{-1} which is observed in the Raman at 115 cm^{-1} in low temperatures [56], but is not resolved at high temperatures. The F mode is also observed at 115 cm^{-1} in the IR [57]. Figure 5 shows the symmetry of the mode and the variation across sillenites. This E mode involves movement of the O(1) atoms and the bismuth atoms. It is important to note that the bismuth and O(1) atoms move in similar directions to each other and therefore the Bi-O(1) force constant between the nearest neighbors may not largely contribute to the frequency. The frequency of this E mode decreases strongly across different sillenites. There is overall only a ∼30% change in width across the compounds, but, compared to other modes, the change is less striking in going from tetravalent to trivalent compounds. The significance of the small change in width will be discussed later in the text.

4. 282 cm^{-1} Raman mode

The strong 282 cm^{-1} Raman mode is easily assigned to an A symmetry due to the polarization properties and the lack of proximal strong modes [56]. DFT calculations resulted in an A mode at 285 cm^{-1} and a 276 cm^{-1} F mode. The latter is weak in the Raman [56], but it was observed in the IR at 288 cm^{-1} [57].

The 282 cm^{-1} A mode has an important symmetry; Fig. 5 shows that the largest contribution to this vibration is the expansion of O(2) atoms away from its 3 Bi nearest neighbors. This Raman peak is a strong probe of the Bi-O(2) bond. Across different sillenites, the frequency of this mode has the strongest dependence on the ionic radius of the metal cation. The dependence can be assigned to the larger unit cells for larger M cations. The width of this mode increases by a factor of 30% and shows some level of disorder for the Bi-O(2) bond.

5. 331 cm^{-1} Raman mode

The 331 cm^{-1} Raman mode observed at 90 K was assigned to the A mode calculated by DFT at 330 cm^{-1}. Polarization measurements by Ramdas show that the strongest peak has A symmetry [56]. The assignment of this mode is straightforward and is useful for comparison across sillenites. Figure 6 shows the Bi-O(1) bending geometry—an important geometry since the frequency should only depend on this bond. The variation across sillenites of the phonon width has a twofold to threefold increase. As will be further discussed below, this mode shows a variation in the Bi-O(1) bond across different sillenites.

6. 546 cm^{-1} Raman mode

The 546 cm^{-1} Raman mode was assigned to the 562 A cm^{-1} mode calculated from DFT. This mode is very straightforward to assign due to its strength and polarization properties [47,56]. This mode is physically important because it only involves Bi-O(1) stretching. (See Fig. 6.) Therefore, this mode is an excellent probe of the Bi-O(1) force constant. Similarly to the Bi-O(1) bending mode, the width of the stretching mode has a large jump from the tetravalent to the trivalent sillenites.

B. Insights into the trivalent sillenites from the strong Raman modes

Assignment and understanding of the symmetry of the six strongest Raman modes present some interesting insight into the trivalent sillenites. The DFT calculations show that the largest contribution to the frequencies of these modes comes from the movement from atoms in the Bi-O framework. The increase in the width of the modes from tetravalent to trivalent sillenites clearly shows that there is an inhomogeneous disorder in trivalent sillenites; that is, there are deviations in the resonant frequencies of these modes across unit cells.

Keeping in mind that these modes are mostly dependent on movement of the Bi, O(1), and O(2) atoms, we will consider two scenarios to explain the large difference in phonon widths between trivalent and tetravalent compounds. First, we can assume that the occupancies of Bi and O(1) and O(2) remain singular in the trivalent sillenites; then the large phonon widths in trivalent sillenites show there are differing Bi-O bond lengths across different unit cells. Distortions or displacements due to the large metal cation may result in distortions of the Bi-O framework. If the model where Bi^{5+} ions sit on the M site is correct [59], then the inhomogeneity may be caused by distorted Bi-O polyhedra in the outside framework.

A second scenario is the existence of O vacancies. O vacancies were suggested by Valant *et al.* to exist in the tetrahedra, O(3) sites, due to the lone pair of Bi^{3+}. Recently, streaks in the electron diffraction pattern of trivalent sillenites [34] also suggest the existence of short-range-ordered O vacancies. However, since the strongest Raman modes are relevant to the Bi-O framework then these modes may have large phonon widths because oxygen vacancies can also exist at the O(1) and O(2) sites. The four easiest modes to assign (132, 282, 331, and 546 cm^{-1}) provide interesting insights. The largest percentage changes (100%–200%) in phonon width occurred in the rocking (331 cm^{-1}) and stretching (546 cm^{-1}) modes of the Bi-O(1) bond. In contrast, the Bi-O(2) bond had a 30% increase in width for the stretching bond. Additional evidence, although weaker, is that the 132 cm^{-1} mode, for which geometry suggests that the frequency should not strongly depend on the Bi-O(1) bond, also had a small increase in phonon width (∼33%). Further evidence is provided by the 626 cm^{-1} E mode (Fig. S1 in the Supplemental Material [48]), which depends mostly on O(1) stretching away from its nearest Bi neighbor and has a large phonon width in the trivalent compounds.

In summary, the strongest conclusion that can be drawn from the Raman spectrum, based on six modes, is that there are O vacancies in the O(1) and O(2) positions that contribute to the large phonon width; a weaker conclusion, based on the comparison of one mode to two modes, is that O(1) vacancies may be more likely than O(2).

C. Other interesting but weak Raman modes

The 626 cm^{-1} mode is absent in the IR and can be easily assigned to the 637 cm^{-1} E mode from the DFT calculations. (Figure S1 in the Supplemental Material [48] shows this vibration.) Previously Mihailova *et al.* assigned this mode mostly to O(3) vibrations based on lattice dynamical calculations. Our DFT calculations show that this mode is

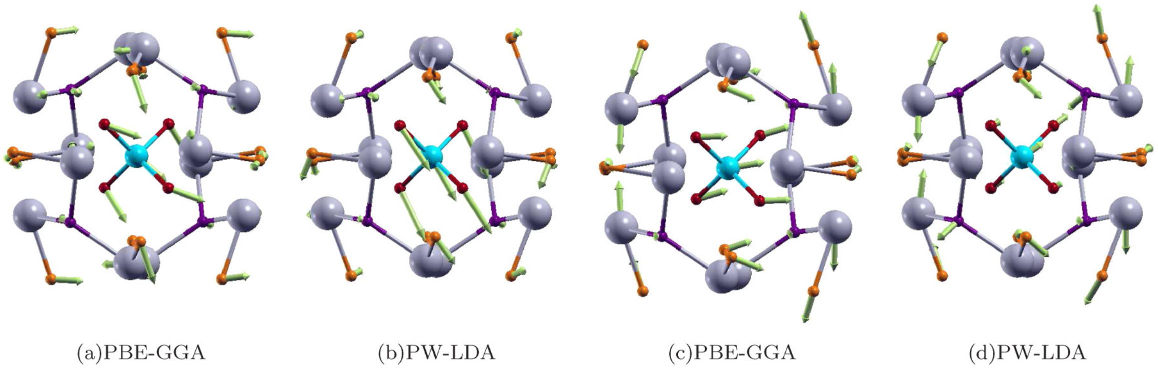

FIG. 7. (Color online) The IR-strong 107 and 136 cm^{-1} F modes. The 107 cm^{-1} mode [(a), (b)] corresponds to displacement of the whole M-O_4 tetrahedron. The 135 cm^{-1} mode [(c), (d)] involves tetrahedron displacement but also movement of both Bi and O(1) atoms. The geometries of the vibrations obtained from [(a), (c)] LDA and [(b), (d)] GGA calculations are both shown. See the text about a discussion on the assignment of these modes. Si and Bi are denoted by blue and gray, respectively; O(1), O(2), and O(3) by orange, purple, and red. Green arrows denote the force on each atom.

mostly from O(2) and O(1) motion. The agreement of our calculations with experiment for the other modes suggests that our assignment is correct. The comparison in width of this mode across sillenites also gives proof of disorder in Bi-O(1) and Bi-O(2) bonds.

Finally, the 785 cm^{-1} A mode in the silicon sillenite corresponds to the symmetric stretching of the tetrahedron. This mode would be an excellent probe of the M-O(3) bond for comparison across sillenites; unfortunately, the mode is already very weak in $Bi_{12}SiO_{20}$, $Bi_{12}GeO_{20}$, and $Bi_{12}TiO_{20}$ and it was not observed in the trivalent sillenites [47].

IV. RESULTS AND DISCUSSION: IR

Here the DFT calculation results will be compared to the experimental IR data on the tetravalent sillenites. Unfortunately, there is no systematic IR study of the trivalent sillenites. Surprisingly, there are also no studies on the tetravalent sillenites that discuss the optical constants (i.e., refractive index or optical conductivity) as well as the intensity and width of the modes. The strongest IR modes were identified based on the 90 K reflectance data from Wojdowski *et al.* [57] and compared to the LDA calculations. We will also discuss a few IR modes with interesting symmetries and show how they could be useful for future IR studies of trivalent sillenites. In this section, when referring to a mode we will use the third column of Table II which corresponds to the IR experimental frequency.

A. Strongest IR modes

1. The 107 and 135 cm^{-1} IR modes

The assignment of these two modes merits extra attention. The DFT calculations predict multiple modes with very similar frequencies in this region. The 107 cm^{-1} mode was assigned to the 111 cm^{-1} frequency predicted by both LDA and GGA. (See Table II.) The IR intensity of this mode was very slow to converge but it was clear it was the strongest in its region. A comparison between the calculated and experimental LO-TO splits aided in the assignment. The 135 cm^{-1} mode was assigned to LDA's 117 and GGA's 121 cm^{-1} modes (Table II). This mode had similar issues; at plane-wave cutoffs smaller than 80 Ry, this mode had a relatively high predicted IR intensity (comparable to the other strong IR modes). However, after 100 Ry, the calculated IR intensity drops to near zero and converges. Fortunately, comparison of the calculated and experimental LO-TO splits were helpful in assigning the mode. Lastly, Fig. 7 shows that the calculation of geometry of vibrations is not trivial; GGA and LDA yielded noticeable differences—but at least the descriptions are overall the same for both functionals.

The geometry of the two modes is shown in Fig. 7. The 107 cm^{-1} vibration corresponds to movement of the whole tetrahedron against the Bi-O framework. The strong infrared response is expected from the geometry of the mode; a large change in polarization results from moving the whole tetrahedron. The 135 cm^{-1} mode also has displacement of the whole tetrahedron as well as movement of the Bi and O(1) atoms. The latter two move in unison and the Bi-O(1) pair moves opposite to the Bi-O(1) pair across the cell.

Since both modes involve displacement of the tetrahedron, their behavior across sillenites could be interesting since trivalent sillenites are expected to have half of the tetrahedrons occupied by a Bi^{3+} cation in the center; therefore, the width of the modes should increase dramatically from the tetravalent to trivalent compounds. Even more interesting would be to measure the width of these phonons for pentavalent compounds; in Valant's stoichiometry model the M site is shared by Bi^{3+}, the M^{5+} cation, and a vacancy, and we therefore expect an even larger jump in phonon width for these compounds.

2. 238, 314, 462, and 531 cm^{-1} IR modes

The next strong IR mode is at 238 cm^{-1}. The geometry of this vibration, and other strong IR modes, is given in the Supplemental Material [48] in Fig. S2. The vibration corresponds to a combination of bending of the Si-O(3) bond and the Bi-O(1) bond. Since O(3) and O(1) vacancies may be present in the trivalent sillenites, a large increase in width is expected for this mode. However, it would be difficult to pinpoint if the width increase is due to O(1), O(3), or both. The IR-strong 314 cm^{-1} (Fig. S2 in the Supplemental Material [48]) also does not have an interesting geometry that would allow probing of a particular bond. For both modes, the biggest change in polarization comes from moving of the positive M cation in a direction opposite to the O(1) anions. The strength of this mode may be attenuated in other sillenites where compounds have an M^{2+}, M^{3+} cation, or a vacancy. The next two strongest IR modes are located at 462 cm^{-1} and 531 cm^{-1}; similarly to the two previous modes, the geometry of the vibrations do not offer a clear probe of a particular bond (Fig. S2 in the Supplemental Material [48]).

3. 822 cm^{-1} IR mode

The 822 cm^{-1} F mode has long been known to correspond to the asymmetric stretching mode of the tetrahedron (Fig. S2 in the Supplemental Material [48]). Unfortunately, this mode is very weak in the Raman spectrum of the tetravalent sillenites and was not observed in the trivalent sillenites. In a systematic IR study of trivalent sillenites, this mode could offer the best probe of the M-O(3) bonds. In a similar prediction for the 135 cm^{-1} mode, a large increase in width, or a peak split, is expected for the divalent and trivalent sillenites due to the larger mass of the Bi^{3+} cation in half of the tetrahedrons. For pentavalent sillenites, a larger increase in width is also expected although the vacant tetrahedrons may not contribute significantly to the IR spectrum due to the lack of a positive cation to contribute to the polarization change.

B. Born effective charges

The low-temperature Raman and infrared spectra of $\text{Bi}_{12}\text{SiO}_{20}$ and $\text{Bi}_{12}\text{GeO}_{20}$ show LO-TO splitting of the F modes [56,57]. However, the cause of the LO-TO splitting was not one of the main focuses of the papers and was only discussed as a product of long-range polarization fields [56]. Other interesting systems with large LO-TO splitting include ferroelectric perovskites such as BaTiO_3 and SrTiO_3 [35,36]. In these perovskites, the Born effective charges ($\mathbf{Z}^*$) have been carefully studied since the effective charges play a role in the LO-TO splitting. The anomalously large Born effective charges, where "large" refers to bigger than the nominal ionic charges, are considered to be indications of ferroelectricity or proximity to a ferroelectric phase transition [37]. Obviously, the perovskites mentioned above are in a tetragonal polar space group and exhibit high ferroelectricity while the sillenites are in a nonpolar space group and do not exhibit ferroelectricity. It is, however, still surprising that the Born effective charges have not been studied in sillenites. It should also be mentioned that recent theoretical studies by Filippetti *et al.* on Born effective charges show that the anomalous charges can be caused by phenomena other than ferroelectricity, such as strong electron correlation [37]; therefore, Born effective charges in systems that exhibit LO-TO splitting remain an interesting topic.

The Born effective charge tensor $\mathbf{Z}^*$ describes the change in total polarization $\vec{P}_{\text{total}}$ caused by the displacement of atoms s:

$$Z^*_{s,i,j} = \frac{\partial P^j_{\text{total}}}{\partial r^i_s}, \tag{2}$$

TABLE III. Born effective charges for each ion calculated along different directions for $\text{Bi}_{12}\text{SiO}_{20}$. The charges were calculated using both the PBE-GGA and PW-LDA functionals. Both functionals predict large anomalous and highly anisotropic Born effective charges for the Bi, O(1), and O(2) ions. Similar results for the Ge sillenite are presented in the Supplemental Material [48].

Ion	Z^*_{LDA}	Z^*_{GGA}	Ion	Z^*_{LDA}	Z^*_{GGA}
Si^{+4}			$\text{O}^{-2}(3)$		
$Z^*_{\text{isotropic}}$	3.23	3.12	$Z^*_{\text{O(3)}\rightarrow\text{Si}}$	−2.77	−2.82
			$Z^*_{\text{O(3)}\rightarrow\text{O(3)}}$	−2.57	−2.70
Bi^{3+}			$\text{O}^{-2}(2)$		
$Z^*_{\text{Bi}\rightarrow\text{O(2)}}$	4.60	4.40	$Z^*_{\text{O(2)}\rightarrow\text{Bi}}$	−3.43	−3.41
$Z^*_{\perp\text{Bi}_3\text{-O(2)}}$	4.50	4.34	$Z^*_{\perp\text{O(2)-Bi}_3}$	−1.34	−1.26
			$Z^*_{\text{O(2)}\rightarrow\text{O(1)}}$	−3.53	−3.50
			$Z^*_{\text{O(2)}\rightarrow\text{O(2)}}$	−2.07	−2.01
			$\text{O}^{-2}(1)$		
$Z^*_{\text{Bi}\rightarrow\text{O(1)}}$	3.46	3.22	$Z^*_{\text{O(1)}\rightarrow\text{Bi}}$	−3.27	−3.34
$Z^*_{\text{Bi}\rightarrow\text{Bi}}$	4.65	4.38	$Z^*_{\text{O(1)}\rightarrow\text{O(1)}}$	−1.81	−1.55

where i and j denote Cartesian coordinates. In BaTiO_3 and SrTiO_3, the Born effective charge of the O anions is anomalously large along the direction away from the Ti^{+4} cation while it is much smaller in the plane perpendicular to this direction [35]. Table III lists the Born effective charges for the $\text{Bi}_{12}\text{SiO}_{20}$ sillenite. The accuracy of the Born effective charges was estimated three ways. First, the convergence of the Born effective charges was checked against the plane-wave cutoff energy and the density of the k mesh; the charges converged within less than 1% at a 100 Ry cutoff energy and a $3 \times 3 \times 3$ k-point mesh. Second, as is common in the literature [49,60], the charge neutrality was checked:

$$\sum_s Z^*{}_{s,i,j} = 0; \tag{3}$$

in other words, summations over all atoms should give a zero Born effective charge in all directions. The LDA calculations resulted in a total isotropic excess charge less than -10^{-3} e per atom. Other authors have reported similar excess charges for unit cells of smaller size [60]. The isotropy of $\sum_s \mathbf{Z}^*$ gives confidence of no direction-dependent errors. The GGA calculations resulted in a larger total (but still small) excess charge of 10^{-2} e per atom. Third, the accuracy of the theoretical predictions was tested by using two different functionals. The values calculated using the GGA and LDA calculations gave very similar results and strengthen our discovery of highly anisotropic and anomalous Born effective charges in $\text{Bi}_{12}\text{SiO}_{20}$. The results also showed, however, that the biggest uncertainty in $\mathbf{Z}^*$ should be attributed to the choice of functionals and not to the calculated excessive charge.

Table III lists the calculated Born effective charges for the various atoms. It is more common to report the Born effective charge for each ion along the interesting directions rather than reporting the whole tensor for each ion [35,37,60]. In this paper, when the charge is reported along a direction $\hat{r}$, the quantity refers to

$$Z^*_{\hat{r}} = \hat{r}^{\dagger}\mathbf{Z}^*_{\mathbf{s}}\hat{r}, \tag{4}$$

and it corresponds to the projection along $\hat{r}$ of the total change of polarization P when the atom is moved in the $\hat{r}$ direction. The projection along $\hat{r}$ is a useful concept that can be related to two simple charges that form a dipole; the change in

TABLE IV. LO-TO splitting calculations for $Bi_{12}SiO_{20}$. The calculations are compared to the experimental values from Refs. [56], [47], and [57]. The PW-LDA and PBE-GGA calculations show good qualitative agreement in predicting which F modes experience the largest LO-TO split in frequency.

LO-TO splitting of F modes in $Bi_{12}SiO_{20}$

Raman freq. [56] (cm^{-1})	IR freq. [57] (cm^{-1})	IR $\Delta_{\text{LO-TO}}$ [57] (cm^{-1})	LDA (cm^{-1})	LDA $\Delta_{\text{LO-TO}}$ (cm^{-1})	GGA (cm^{-1})	GGA $\Delta_{\text{LO-TO}}$ (cm^{-1})
89	89	2	73	<1	83	5
99	98	2	98	<1	95	<1
106	107	5	111	10	111	5
115	115	3	111	<1	103	3
135	136	32	121	19	117	24
171	175	10	163	<1	164	<1
196	195	1	187	<1	206	<1
209	208	4	206	2	218	2
252	237	20	235	19	245	16
n.o.	288	37	282	12	276	7
n.o.	314	37	330	21	326	18
352	353	21	374	19	372	11
464	462	44	488	31	471	32
n.o.	531	26	550	28	532	34
n.o.	579	22	602	<1	590	<1
n.o.	609	11	606	11	604	13
827	822	16	841	11	795	14

polarization along $\hat{r}$ is proportional to the charge of the ion when the ion is moved in that direction.

The plane formed by the three bismuth atoms bonded to O(2) shows interesting Born effective charges. $Z^*_{\hat{r}}$ for bismuth is around 4.5 in the direction of Bi towards the O(2) atom. Compare this 1.5 Born/nominal ratio to the 1.8 ratio observed for Ti^{4+} in the $BaTiO_3$ ferroelectric perovskite and other similar compounds [60]. Moreover, the Born/nominal ratio of O(2) in the direction towards any of the nearby Bi is also anomalous at 1.7. The anomaly for O(2) is more interesting for the direction perpendicular to the Bi_3 plane where the Born/nominal ratio drops to 0.65. Such a large change with directions of $Z^*_{\hat{r}}$ is also observed in the octahedral O ions of perovskite ferroelectrics [60]. In these compounds, however, the Born/nominal ratio of the oxygens does not reach such a small value [35].

The Bi-O(1) bond also shows anomalous charges as shown in Table III. The effective charge of O(1) in the direction towards another nearby O(1) was however not anomalous. Finally the O(3) Born effective charges were much more isotropic and with smaller Born/nominal ratios. Table S2, in the Supplemental Material [48], shows various $Z^*_{\hat{r}}$ for the $Bi_{12}GeO_{20}$ sillenite and shows that this compound also has anomalous and highly anisotropic Born effective charges.

As a final note, the significance of the large value of Born effective charges would be better understood if calculations were made for many different Bi compounds with various known physical characteristics (strong correlation, ferroelectric, etc.). The largest number of Born effective charge calculations have been made on ferroelectric compounds and these compounds all show anomalous $\mathbf{Z}^*$. However, there are not many reports of Born effective calculations on other systems that do not show an anomalous value; therefore, it is difficult to argue the importance of anomalous $\mathbf{Z}^*$s if there are not many reports for systems with normal $\mathbf{Z}^*$. The authors plan to work on a comprehensive study of the Born effective charges of various Bi oxides.

C. LO-TO splitting

In this report, the large anomalous Born effective charges are reported to indicate that they play a role in the splitting of LO-TO modes. The term in the dynamical matrix responsible for the splitting is a direction-dependent term valid only at the Γ point, $q = [0,0,0]$, that involves the Born effective charges for each atom (s) along a chosen direction $Z^*_{s'\hat{r}}$ and the high-frequency dielectric constant ϵ_∞,

$$D_{ss'} = \frac{4\pi e^2}{\Omega}\frac{Z^*_{s\hat{r}} Z^*_{s'\hat{r}}}{\epsilon_\infty}. \tag{5}$$

Each matrix term is direction dependent due to the tensor nature of $\mathbf{Z}^*$. For our cubic crystal, the calculated LO-TO splitting was independent of the chosen direction. Table IV shows the experimental splits in frequency between the LO and TO modes, $\Delta_{\text{LO-TO}}$, from the 90 K $Bi_{12}SiO_{20}$ infrared data from Wojdowski *et al.* [56,57]. The infrared analysis by Wojdowski calculates the frequency of the TO modes by finding the maxima in the imaginary permittivity $\text{Im}\{\epsilon(\omega)\}$ and calculates the frequency of the LO modes by using the loss function $\text{Im}\{\frac{1}{\epsilon(\omega)}\}$ [57]. Since the results are dependent on Kramers-Kronig analysis, a certain error is expected. Table IV also shows the magnitude of the splits calculated using a norm-conserving pseudopotential and both LDA and GGA functionals. The numerical agreement between the calculated values and the experimental values is poor; however, the LDA calculations at least predict which modes will have the strongest splits. The qualitative agreement further strengthened the assignment of some of the modes. Finally, the high-frequency dielectric constant calculated using LDA was 6.2, and 5.9 for GGA, close to the experimental value, 6.3, obtained from reported optical measurements [61]. The convergence of ϵ_∞ was within less than 1% at a k mesh of $3 \times 3 \times 3$ and a 100 Ry cutoff for plane waves.

V. ADDITIONAL DISCUSSION

A. Comparison with lattice dynamical calculations

It is interesting to compare our DFT results to the lattice dynamical (LD) calculations presented by previous authors in the literature. Both methods have advantages and disadvantages and they should therefore be considered complementary. Lattice dynamical calculations use the experimental frequencies of the spectra to calculate the force constants between atoms; then, the force constants are used to recalculate the vibrational frequencies and are compared to experiment. The method is useful in using force constants from strong and well-known modes and then calculating weaker and more complicated vibrations. A variation of the method uses a potential model for each atom; but, the idea is the same because several parameters for the potential are varied until it agrees with experiment. Lattice dynamical calculations provide a lot of insight into many systems such as perovskites [62–65], pyrochlores [66–68], and sillenites [69,70].

LD calculations also have their weaknesses. In practice, several parameters are calculated from a small number of known variables. Such calculations raise concerns if there is only one combination of multiple force constants that would predict the observed frequencies. Furthermore, the number of springs or terms in the potential are also variable. The technique has been very useful but it has its difficulties. In some pyrochlore compounds, the highest-frequency Raman peak is observed around 600 cm^{-1}. Lattice dynamical calculations yielded force constants that agreed with experiment but predicted the highest mode around 600 cm^{-1}. Afterwards, many studies assigned higher-frequency modes in other pyrochlores to overtones or bands. Lately, experimental and DFT studies have shown that the highest-frequency mode in some pyrochlores can far exceed this frequency [31,44,45]. Such reassignments are not trivial since the highest-frequency mode is useful for some nonlinear applications [71].

DFT calculations offer an impressive advantage in that the structure is built using pseudopotentials specific for each atom; the structure is relaxed towards the lowest-energy configuration, and the phonon frequencies are calculated without biasing the results towards known optical spectra. The pseudopotentials available online for the atoms studied in this compound have been tested for not only phonon calculations, but also other applications. Therefore, DFT offers higher potential for predictions. However, DFT is not without its disadvantages. Different choices of approximations in the pseudopotentials can yield different results. The use of different pseudopotentials in this work was important in making the right conclusions.

B. Relevance and future work

The analysis of the Raman data across different sillenites suggests the existence of O vacancies in the Bi-O framework. These vacancies would be difficult to detect with x-ray measurements since bismuth is a stronger scatterer than oxygen based due to their atomic numbers. Furthermore, no previous Rietveld refinements were performed assuming O(1) vacancies or Bi-O(1) distortions. In the trivalent sillenites, it was expected that the large M cation, and the Bi^{3+} cation, would distort the tetrahedron, and the lone pair of Bi^{3+} would result in O(3) vacancies only. Future studies of the trivalent sillenites using neutron scattering may provide additional insight since the scattering from oxygen atoms would not be so weak compared to bismuth.

The stoichiometry model by Valant *et al.*, which describes in detail the occupation of the M site for various metal valences, could be further corroborated by a systematic study of the IR spectra of different sillenites. As discussed earlier in the text, some modes such as the tetrahedron displacement could show splitting of frequencies for divalent, trivalent, and pentavalent sillenites. The intensity of the split modes could also be related to the occupation of the M site.

The accuracy of both the LDA and GGA calculations in the sillenites strengthens the confidence of DFT calculations in other systems. In the Bi pyrochlores, there are strong Raman peaks around 750 cm^{-1}, uncharacteristic of second-order Raman scattering [31], that put doubt on the traditional assignment of modes above 600 cm^{-1} as an overtone. DFT calculations on $\mathrm{Bi_2Ti_2O_7}$ by Patterson *et al.* [31,72] and Ti pyrochlores by Kumar and Gupta [44,45] suggest that the 750 cm^{-1} mode is a fundamental and not an overtone. The relative accuracy of the LDA functional on sillenites, average variance of 3%, gives confidence that the LDA phonon calculations on pyrochlores [45,72] are not incorrect by 25% of the experimental frequency. In this case, the prediction by Patterson *et al.* that the highest frequency mode for a Bi pyrochlore is 711 cm^{-1} agrees well with the experimental data [31]. It would also be interesting to restudy these systems using the PBE-GGA functionals and see what the highest predicted frequency is for a fundamental mode.

VI. CONCLUSIONS

The vibrational frequencies of $\mathrm{Bi_{12}SiO_{20}}$ were studied using DFT with norm-conserving pseudopotentials and both PW-LDA and PBE-GGA functionals. Unlike reports on other metal oxides, GGA outperformed LDA in structural calculations. Both the IR and Raman scattering cross sections were calculated and the LDA functional successfully predicted which modes should be the strongest in the experimental spectra. The assignment of the modes allows understanding of the geometry of the vibrations and the understanding can be used to understand patterns across different sillenites. The large phonon widths in vibrations involving Bi-O(1) and Bi-O(2) bonds are evidence of inhomogeneous disorder in the Bi-O framework and suggest O vacancies at the O(1) and/or O(2) positions. The careful discussion on $\mathrm{Bi_{12}SiO_{20}}$ about the convergence of physical values for a large system, the use of different pseudopotentials, and the use of two different sum rules may be useful for the study of other metal oxides.

ACKNOWLEDGMENTS

D.J.A. would like to thank the Institute of Scientific and Industrial Research at Osaka University for support. A.F.K. was supported by the Laboratory Directed Research and Development Program of Lawrence Berkeley National Laboratory under U.S. Department of Energy Contract No. DE-AC02-05CH11231. The authors also thank J. Hoskins and M. Lufaso for useful discussions.

---

[1] E. L. Venturini, E. G. Spencer, and A. A. Ballman, J. Appl. Phys. **40**, 1622 (1969).
[2] M. Peltier and F. Micheron, J. Appl. Phys. **48**, 3683 (1977).
[3] P. Refregier, L. Solymar, H. Rajbenbach, and J. Huignard, J. Appl. Phys. **58**, 45 (1985).
[4] H. C. Pedersen, D. J. Webb, and P. M. Johansen, J. Opt. Soc. Am. B **15**, 2573 (1998).
[5] M. I. Castillo, P. M. Aguilar, J. Sanchez-Mondragon, S. Stepanov, and V. Vysloukh, Appl. Phys. Lett. **64**, 408 (1994).
[6] A. Fox and T. Bruton, Appl. Phys. Lett. **27**, 360 (2008).
[7] W. Wei, Y. Dai, and B. Huang, J. Phys. Chem. C **113**, 5658 (2009).
[8] X. Zhu, J. Zhang, and F. Chen, Appl. Catal., B **102**, 316 (2011).
[9] W. Guo, Y. Yang, Y. Guo, Y. Jia, H. Liu, and Y. Guo, Phys. Chem. Chem. Phys. **16**, 2705 (2014).
[10] G.-Q. Tan, Y.-Q. Zheng, H.-Y. Miao, A. Xia, and H.-J. Ren, J. Am. Ceram. Soc. **95**, 280 (2012).
[11] A. Sun, H. Chen, C. Song, F. Jiang, X. Wang, and Y. Fu, RSC Adv. **3**, 4332 (2013).
[12] R. Köferstein, T. Buttlar, and S. G. Ebbinghaus, J. Solid State Chem. **217**, 50 (2014).
[13] P. Petkova, Opt. Mater. **37**, 160 (2014).
[14] H. Sekhar and D. N. Rao, J. Mater. Sci.: Mater. Electron. **24**, 1569 (2013).
[15] T. Elkhouni, M. Amami, and A. B. Salah, J. Supercond. Novel Magn. **26**, 2997 (2013).
[16] V. Marinova, R. C. Liu, S. H. Lin, and K. Y. Hsu, Optics Lett. **36**, 1981 (2011).
[17] S. Simon and A. D. Udvar, J. Am. Ceram. Soc. **93**, 2760 (2010).
[18] L. A. S. de Oliveira, J. P. Sinnecker, M. D. Vieira, and A. Penton-Madrigal, J. Appl. Phys. **107**, 09D907 (2010).
[19] A. Kokalj, J. Mol. Graphics Modell. **17**, 176 (1999).
[20] M. Valant and D. Suvorov, Chem. Mater. **14**, 3471 (2002).
[21] X. Xi, J. Hwang, C. Martin, D. B. Tanner, and G. L. Carr, Phys. Rev. Lett. **105**, 257006 (2010).
[22] X. Xi, Y. M. Dai, C. Homes, M. Kidszun, S. Haindl, and G. L. Carr, Phys. Rev. B **87**, 180509 (2013).
[23] C.-C. Chen, C. J. Jia, A. F. Kemper, R. R. P. Singh, and T. P. Devereaux, Phys. Rev. Lett. **106**, 067002 (2011).
[24] G. R. Boyd, T. P. Devereaux, P. J. Hirschfeld, V. Mishra, and D. J. Scalapino, Phys. Rev. B **79**, 174521 (2009).
[25] A. Akrap, J. J. Tu, L. J. Li, G. H. Cao, Z. A. Xu, and C. C. Homes, Phys. Rev. B **80**, 180502 (2009).
[26] K. H. Miller, X. S. Xu, H. Berger, V. Craciun, X. Xi, C. Martin, G. L. Carr, and D. B. Tanner, Phys. Rev. B **87**, 224108 (2013).
[27] K. H. Miller, P. W. Stephens, C. Martin, H. Berger, G. L. Carr, and D. B. Tanner, Phys. Rev. B **86**, 174104 (2012).
[28] K. H. Miller, X. S. Xu, H. Berger, E. S. Knowles, D. J. Arenas, M. W. Meisel, and D. B. Tanner, Phys. Rev. B **82**, 144107 (2010).
[29] C. Turner, P. M. Johns, E. M. Thatcher, D. B. Tanner, and J. C. Nino, J. Phys. Chem. C **118**, 28797 (2014).
[30] M. Chen, D. B. Tanner, and J. C. Nino, Phys. Rev. B **72**, 054303 (2005).
[31] D. J. Arenas, L. V. Gasparov, W. Qiu, J. C. Nino, C. H. Patterson, and D. B. Tanner, Phys. Rev. B **82**, 214302 (2010).
[32] Y. Zhang, Z. Zhang, X. Zhu, Z. Liu, Y. Li, and T. Al-Kassab, Appl. Phys. A **115**, 661 (2014).
[33] P. Ning, L. Li, X. Zhang, M. Wang, and W. Xia, Mater. Lett. **87**, 5 (2012).
[34] C. A. Scurti, N. Auvray, M. W. Lufaso, S. Takeda, H. Kohno, and D. Arenas, AIP Adv. **4**, 087125 (2014).
[35] W. Zhong, R. D. King-Smith, and D. Vanderbilt, Phys. Rev. Lett. **72**, 3618 (1994).
[36] P. Ghosez, X. Gonze, P. Lambin, and J.-P. Michenaud, Phys. Rev. B **51**, 6765 (1995).
[37] A. Filippetti and N. A. Spaldin, Phys. Rev. B **68**, 045111 (2003).
[38] B. B. Hinojosa, J. C. Nino, and A. Asthagiri, Phys. Rev. B **77**, 104123 (2008).
[39] P. Giannozzi, S. Baroni, N. Bonini, M. Calandra, R. Car, C. Cavazzoni, D. Ceresoli, G. L. Chiarotti, M. Cococcioni, I. Dabo, A. D. Corso, S. de Gironcoli, S. Fabris, G. Fratesi, R. Gebauer, U. Gerstmann, C. Gougoussis, A. Kokalj, M. Lazzeri, L. Martin-Samos, N. Marzari, F. Mauri, R. Mazzarello, S. Paolini, A. Pasquarello, L. Paulatto, C. Sbraccia, S. Scandolo, G. Sclauzero, A. P. Seitsonen, A. Smogunov, P. Umari, and R. M. Wentzcovitch, J. Phys.: Condens. Matter **21**, 395502 (2009).
[40] J. P. Perdew, K. Burke, and M. Ernzerhof, Phys. Rev. Lett. **77**, 3865 (1996).
[41] L. Wiehl, A. Friedrich, E. Haussühl, W. Morgenroth, A. Grzechnik, K. Friese, B. Winkler, K. Refson, and V. Milman, J. Phys.: Condens. Matter **22**, 505401 (2010).
[42] H. Deng, W. Hao, and H. Xu, Rare Met. **30**, 135 (2011).
[43] S. A. Farias and J. B. L. Martins, Chem. Phys. Lett. **533**, 78 (2012).
[44] S. Kumar and H. Gupta, Vib. Spectrosc. **62**, 180 (2012).
[45] S. Kumar and H. Gupta, Solid State Sci. **14**, 1405 (2012).
[46] H. J. Monkhorst and J. D. Pack, Phys. Rev. B **13**, 5188 (1976).
[47] D. J. Arenas, T. Jegorel, C. Knab, L. V. Gasparov, C. Martin, D. M. Pajerowski, H. Kohno, and M. W. Lufaso, Phys. Rev. B **86**, 144116 (2012).
[48] See Supplemental Material at http://link.aps.org/supplemental/10.1103/PhysRevB.91.144103 for additional tables and figures. The Supplemental Material contains a table comparing the structural parameters for $Bi_{12}SiO_{20}$ predicted by PBE-GGA and PW-LDA, additional figures for the geometry of phonon modes, and the results from phonon and born-charges calculations for $Bi_{12}GeO_{20}$.
[49] J. Pruneda and E. Artacho, Phys. Rev. B **72**, 085107 (2005).
[50] Z. Wu and R. E. Cohen, Phys. Rev. B **73**, 235116 (2006).
[51] Z. Wu, R. E. Cohen, and D. J. Singh, Phys. Rev. B **70**, 104112 (2004).
[52] M. Cococcioni, A. Dal Corso, and S. de Gironcoli, Phys. Rev. B **67**, 094106 (2003).

[53] N. N. F. Mounet, Ph.D. thesis, Massachusetts Institute of Technology, 2005.

[54] N. Mounet and N. Marzari, Phys. Rev. B **71**, 205214 (2005).

[55] M. Lazzeri and F. Mauri, Phys. Rev. Lett. **90**, 036401 (2003).

[56] S. Venugopalan and A. K. Ramdas, Phys. Rev. B **5**, 4065 (1972).

[57] W. Wojdowski, T. Łukasiewicz, W. Nazarewicz, and J. Żmija, Phys. Status Solidi B **94**, 649 (1979).

[58] W. Wojdowski, Phys. Status Solidi B **130**, 121 (1985).

[59] D. Craig and N. Stephenson, J. Solid State Chem. **15**, 1 (1975).

[60] F. Detraux, P. Ghosez, and X. Gonze, Phys. Rev. B **56**, 983 (1997).

[61] L. Escobar-Alarcon, E. Haro-Poniatowski, M. Fernandez-Guasti, A. Perea, C. N. Afonso, and T. Falcon, Appl. Phys. A **69**, S949 (1999).

[62] H. Gupta, P. Ashdhir, and C. Rawat, J. Phys. Chem. Solids **57**, 1857 (1996).

[63] M. V. Abrashev, A. P. Litvinchuk, M. N. Iliev, R. L. Meng, V. N. Popov, V. G. Ivanov, R. A. Chakalov, and C. Thomsen, Phys. Rev. B **59**, 4146 (1999).

[64] H. Gupta, M. Kumar Singh, and L. Tiwari, J. Raman Spectrosc. **33**, 67 (2002).

[65] R. Silva, H. Reichlova, X. Marti, D. Barbosa, M. Lufaso, B. Araujo, A. Ayala, and C. Paschoal, J. Appl. Phys. **114**, 194102 (2013).

[66] S. Brown, H. Gupta, J. Alonso, and M. Martinez-Lope, J. Raman Spectrosc. **34**, 240 (2003).

[67] S. Saha, D. V. S. Muthu, C. Pascanut, N. Dragoe, R. Suryanarayanan, G. Dhalenne, A. Revcolevschi, S. Karmakar, S. M. Sharma, and A. K. Sood, Phys. Rev. B **74**, 064109 (2006).

[68] H. Gupta, J. Singh, S. Kumar, N. Rani *et al.*, J. Mol. Struct. **937**, 136 (2009).

[69] B. Mihailova, M. Gospodinov, and L. Konstantinov, J. Phys. Chem. Solids **60**, 1821 (1999).

[70] B. Mihailova, G. Bogachev, V. Marinova, and L. Konstantinov, J. Phys. Chem. Solids **60**, 1829 (1999).

[71] J. Zhao, N. Qin, and D. Bao, J. Am. Ceram. Soc. **96**, 3768 (2013).

[72] C. H. Patterson, Phys. Rev. B **82**, 155103 (2010).